



Defects induced efficient overall water splitting on a carbon-based metal-free photocatalyst

Cheng Zhu^a, Mengmeng Zhu^a, Yue Sun^a, Yunjie Zhou^a, Hui Huang^a, Yeshayahu Lifshitz^{a,b},
Shuit-Tong Lee^a, Jun Zhong^{a,*}, Yang Liu^{a,*}, Zhenhui Kang^{a,*}

^a Jiangsu Key Laboratory for Carbon-Based Functional Materials & Devices, Institute of Functional Nano & Soft Materials (FUNSOM), Soochow University, 199 Ren'ai Road, Suzhou, 215123, Jiangsu, PR China

^b Department of Materials Science and Engineering, Technion, Israel Institute of Technology, Haifa, 3200003, Israel

ARTICLE INFO

Keywords:

Metal-free carbon based photocatalysts
Overall water splitting
Controllable carbon defects
Defects as oxidation sites
Selectable electron pathway

ABSTRACT

Hydrogen production from overall water splitting by photocatalyst is an ultimate clean and renewable energy strategy. Recent developments show that carbon based materials are considerable photocatalysts for overall water splitting under visible light because of their high activity, high stability, low-cost, easy fabrication and structural diversity. However, it still lacks a systematic study and deep understanding on the working mechanism of the carbon based photocatalysts. Herein, we show the fabrication of a carbon photocatalyst with abundant carbon defects created by removing the nitrogen atoms from a N-doped precursor. The active defects bond with water molecules during the photocatalytic reaction, which then work as oxidation sites for O₂ generation. We also demonstrate an accessible strategy to produce more defects to observably enhance the photocatalytic activity (around 10 times) as well as to select between the 2-electron/2-electron and the 4-electron pathway water splitting. The synthesized photocatalyst is efficient in photocatalytic visible-light overall water splitting with an optimum H₂ and O₂ production of 2.54 and 1.25 μmol h⁻¹, respectively. Moreover, the quantum efficiency and solar to hydrogen (STH) efficiency were measured to be 2.04% for wavelength λ = 420 ± 20 nm and 0.1% using AM 1.5 G, respectively.

1. Introduction

Photocatalytic overall water splitting into H₂ and O₂ (requires free energy as high as 113.38 kcal/mol) is a considerable and amenable approach to produce clean energy without any contamination [1–3]. The essentially existent challenges for the photocatalytic overall water splitting are the formation of O–O bond and the following release of diatomic O₂ molecules, which involve the coupling of four electrons and the transfer of four protons [4]. Photocatalytic overall water splitting can occur via either the stepwise two-electron pathway (1: 2H₂O → H₂O₂ + H₂ 2: 2H₂O₂ → O₂ + 2H₂O) or the one-step four-electron pathway (2H₂O → 2H₂ + O₂), wherein the four-electron process for O₂ evolution (1.23 eV) is thermodynamically superior to the two-electron process for H₂O₂ formation (1.78 eV) [5]. Nonetheless, the kinetically competing two-electron reaction into H₂O₂ is somehow easier to occur. Therefore, it remains a challenge to modulate the electron pathway so as to improve the energy utilization and conversion.

Tremendous efforts have been devoted to exploiting and developing various semiconductors as water splitting photocatalysts [6–8].

However, some metal-containing semiconductors as overall water splitting photocatalysts still suffer from the limits like high cost, environment hazards, poor stability, intrinsic deficiency of band positions and low utilization of visible light [9–13]. Carbon based materials are potential alternatives to metal-containing semiconductors because of their all-round merits, such as earth-abundance, molecular level design, devisable structure, ease of multiple doping, low cost and non-pollution [14,15]. Carbon based overall water splitting photocatalysts screamed into people's eyes when graphite oxide was reported for photocatalytic overall water splitting [16,17]. Later on, two carbon nitride systems were successfully constructed for photocatalytic overall water splitting with outstanding activity and high efficiency [18,19]. Recently, conjugated microporous polymers were also designed from the molecular level, which have suitable bandgaps for generating H₂ and O₂ simultaneously under visible light irradiation [20]. The performance of carbon based overall water splitting photocatalysts has signified that carbon based materials are prospective candidates for cost-effective and large-scale overall water splitting. As a result, it is urgent not only to explore more carbon based photocatalysts but also intensively progress

* Corresponding authors.

E-mail addresses: jzhong@suda.edu.cn (J. Zhong), yangl@suda.edu.cn (Y. Liu), zhkang@suda.edu.cn (Z. Kang).

<https://doi.org/10.1016/j.apcatb.2018.05.071>

Received 9 March 2018; Received in revised form 9 May 2018; Accepted 24 May 2018

Available online 26 May 2018

0926-3373/ © 2018 Elsevier B.V. All rights reserved.

in profound mechanism research.

Defects, especially the intrinsic defects in catalysts are considered effective to enhance the catalytic properties [21–24]. A number of works have figured out defects in carbon nitride not only improve charge separation but also enhance visible-light absorbance for photocatalytic water splitting [25–27]. No work, however, has been reported to discuss the defect chemistry in normal carbon based metal-free photocatalysts. Here, a metal-free photocatalyst (NCN/CDs) was designed with intrinsic carbon defects by a facile nitrogen removal procedure from a N-doped precursor. The introduction of carbon dots (CDs) is favorable for rapid charge separation and efficient gases production. On the one hand, the defects can bond with the adsorbed H_2O molecules to work as oxidation sites for O_2 generation; on the other hand, CDs work as reduction sites to accept electrons for H_2 release. In addition, we manage to create more carbon defects by removing nitrogen species under higher annealing temperature to enhance the photocatalytic activity (around 10 times for the optimized one). Particularly, when the nitrogen content is lower than 10% the catalyst proceeds a 4-electron pathway, while it tends to take a 2-electron/2-electron pathway when the nitrogen content is higher than 10%. The synthesized NCN/CDs samples are active in photocatalytic overall water splitting under visible light ($\lambda > 420 \text{ nm}$) with the optimal evolution rate of H_2 and O_2 to be $2.54 \mu\text{mol h}^{-1}$ and $1.25 \mu\text{mol h}^{-1}$, respectively. Besides, the service lifetime of the NCN/CDs photocatalysts was measured to be more than 500 h.

2. Experimental section

2.1. Materials synthesis

All the reagents were purchased from Adamas-beta® without extra purification before usage. CDs were synthesized according to our previous reports [28,29]. Typically, 10 mL aniline (ANI, 0.1 mol L^{-1}) purified by distillation previously was put into a 100 mL beaker. Later on, the mixture of 10 mL ammonium persulfate ($\text{H}_8\text{N}_2\text{O}_8\text{S}_2$, 0.1 mol L^{-1}), 10 mL hydrochloric acid (HCl, 0.1 mol L^{-1}) and 1 mg CDs was injected drop by drop into ANI. Subsequently, a piece of clean melamine foam (MF) was put into the beaker to adsorb the whole solution. The reactant was then put standing in air condition for 3 days for *in-situ* polymerization. Finally, the moisture in the emeraldine precursor was removed by freeze-drying (SCIENTZ-10 N, SCIENTZ BIOTECHNOLOGY CO., LTD.) with rapid freezing at -78°C followed by vacuum desiccation for 3 days. After that, the as-prepared precursor was then pyrolyzed in a tube furnace with Ar flow at 600, 700, 800, 900, 1000, and 1100°C , respectively. The thermal insulation process was kept for 120 min following by natural cooling to the room temperature. Afterwards, the obtained samples (denoted as NCN/CDs-600, NCN/CDs-700, NCN/CDs-800, NCN/CDs-900, NCN/CDs-1000 and NCN/CDs-1100 accordingly) were grinded evenly and washed using deionized water for 3 times.

2.2. Materials characterization

Transmission electron microscopy (TEM), high-resolution transmission electron microscopy (HRTEM) and high angle annular dark field-scanning transmission electron microscope (HAADF-STEM) were measured by using a FEI-Tecnai F20 transmission electron microscope with an accelerating voltage of 200 kV. The size distribution was measured by dynamic light scattering (DLS) on a Malvern ZEN3690. The scanning electron microscope (SEM) was applied to characterize the surface morphology and element contents of the samples. The fourier transform infrared (FTIR) spectrum of the samples was acquired from a Hyperion spectrophotometer (Bruker) at the scan range of $400\text{--}4000 \text{ cm}^{-1}$. UV/VIS/NIR spectrophotometer (Lambda 750, Perkinelmer) was employed to acquire the UV-vis absorption spectra. Raman spectra were collected by using a HR 800 Raman spectroscopy

(JY, France) with a 20 mW air-cooled argon ion laser (633 nm) as the excitation source. Powder X-ray diffraction (XRD) was carried out to characterize the crystal structure of the as-prepared products by using a PIXcel3D X-ray diffractometer (Empyrean, Holland Panalytical) with Cu K α radiation ($\lambda = 0.154178 \text{ nm}$). X-ray photoelectron spectroscopy (XPS) measurements were conducted on a KRATOS Axis ultra-DLD X-ray photo-electron spectroscope with a monochromatic Al K α X-ray source ($h\nu = 1283.3 \text{ eV}$). All the electrochemical measurements were conducted on a CHI 920C workstation (CH Instruments, Shanghai, China), using a standard three-electrode system, of which a platinum wire is used as the counter electrode, a saturated calomel electrode (SCE) as the reference electrode and a glass carbon (GC) electrode as working electrode. Electrochemical impedance spectra (EIS) measurements were carried out at open circuit potential as well, with a frequency range from 1 MHz to 0.01 Hz and an AC voltage amplitude of 5 mV in ultrapure water. A Horiba Jobin Yvon (Fluoro Max-4) luminescence spectrometer was employed to record the photoluminescence (PL) spectra. X-ray absorption spectra (XAS) were collected at the Beijing Synchrotron Radiation Facility (BSRF, Soft X-ray beamline) and the National Synchrotron Radiation Laboratory (NSRL, XMCD beamline).

2.3. Water splitting test

The photocatalytic property of the as-prepared samples was evaluated using (300 W Xe-lamp, PLS-SXE 300, Beijing Trusttech Co. Ltd, China), either a bandpass or a long-pass cutoff filter to get specific wavelength visible light ($\lambda = 420 \pm 20 \text{ nm}$, $460 \pm 20 \text{ nm}$, $500 \pm 20 \text{ nm}$, $540 \pm 20 \text{ nm}$, $580 \pm 15 \text{ nm}$, and $600 \pm 10 \text{ nm}$ etc.) or the wide range visible light ($\lambda \geq 420 \text{ nm}$). No sacrificial agents were needed. In a typical process, 100 mg of the as-prepared sample was dispersed in 100 mL ultrapure water by ultrasonic dispersion for at least 30 min to get a homogenous suspension. Then the suspension was transferred to a Pyrex glass photoreactor (equipped with a flat window at the top for illumination, and a magneton at the bottom), which was connected to an enclosed gas-circulation system. Afterwards, the system was degassed to completely remove air (including dissolved air). The temperature of the mixed liquor was maintained at 25°C by cyclic water installation during the photocatalytic reaction. To detect the gas production, a gas chromatograph (SP-7890) set up with a 5 \AA molecular sieves column and a thermal conductivity detector (TCD) was utilized. Nitrogen was used as the carrier gas with the flow rate of 30 mL min^{-1} .

2.4. Electrochemical characterization of electron structure

Cyclic voltammetry (CV) was operated using a standard three-electrode system with CHI 920C workstation (CH Instruments, Shanghai). A platinum (Pt) wire and an Ag/AgCl (3 M KCl) electrode were used as the counter electrode and the reference electrode, respectively. A glassy carbon (GC) electrode (3 mm diameter) was thoroughly cleaned by polishing to mirror finish, and dried before further use. $10 \mu\text{L}$ catalyst solution (1 mg mL^{-1}) and $5 \mu\text{L}$ of 0.5 wt % Nafion solution were dropped onto the working area of a cleaned GC electrode and put naturally to dry. The CV curves were measured in N_2 -saturated 0.1 M BMIMPF₆ solution with a scan rate of 50 mV s^{-1} . Ferrocene was added into the above solution as an internal standard with a concentration of 1 mg mL^{-1} . The HOMO and LUMO energy levels were calculated from the onset of oxidation (E_{ox}), reduction (E_{red}) potentials and the reference energy level for ferrocene (4.8 eV below the vacuum level) as determined by CV according to the equations:

$$E_{\text{HOMO}} = -(E_{\text{onset}}^{\text{ox}} - E_{\text{fe}} + 4.80) \text{ eV} \quad (1)$$

$$E_{\text{LUMO}} = -(E_{\text{onset}}^{\text{red}} - E_{\text{fe}} + 4.80) \text{ eV} \quad (2)$$

$$E_{\text{g}} (\text{band gap}) = E_{\text{onset}}^{\text{ox}} - E_{\text{onset}}^{\text{red}} \quad (3)$$

where E_{fe} is the onset of the oxidation potential (vs. Ag/AgCl) of ferrocene.

2.5. Determination of electron transfer number

The electron transfer number was determined via rotating disk-ring electrodes (RRDE) testing system (RRDE-3 A, ALS Co., Ltd). RRDE experiments were carried out in ultrapure water (N_2 saturated) with a scan rate of 10 mV s^{-1} and rotating speed of 1600 rpm. The disk potential was set at open circuit potential to avoid electrochemical catalysis process for water oxidation. The ring potential was kept at 0.9 V vs. SCE, which can oxidize the generated H_2O_2 from the disk into O_2 . All the process and data were recorded by a CHI 920C electrochemical workstation (CH Instruments, Shanghai, China).

The electron transfer number (n) was evaluated according to the following equation:

$$n = \frac{4I_d}{I_d + I_r/N} \quad (4)$$

In the formula, I_d and I_r represent the disk and ring current, respectively, while N is the RRDE collection efficiency determined to be 0.24.

2.6. Calculation of apparent quantum efficiency (AQY)

The catalyst solution was irradiated by a 300 W Xe lamp applying a band-pass filter ($\lambda_0 = 420 \pm 20\text{ nm}$, $460 \pm 20\text{ nm}$, $500 \pm 20\text{ nm}$, $540 \pm 20\text{ nm}$, $580 \pm 15\text{ nm}$, and $600 \pm 10\text{ nm}$, respectively) for 12 h. The average intensity of irradiation was determined to be 8 mW cm^{-2} by an ILT 950 spectroradiometer (International Light Technologies) and the irradiation area was 0.785 cm^2 . The number of incident photons (N) is calculated by Eq. (5).

$$N = \frac{E\lambda}{hc} \quad (5)$$

In Eq. (5), E is the average intensity of irradiation, λ stands for the wavelength of the irradiation, h represents the Planck constant and c is the speed of light.

The quantum efficiency is calculated from Eq. (6).

$$AQE = \frac{2 \times \text{the number of evolved } H_2 \text{ molecules}}{\text{the number of incident photons}} \times 100\% \quad (6)$$

2.7. Calculations of solar to hydrogen (STH) conversion efficiency from solar simulator measurements

The solar energy conversion was evaluated by using AM 1.5 G solar simulator as the light source with NCN/CDs-1000 ($0.025\text{ g}_{\text{CDs}}/\text{g}_{\text{catalyst}}$) as the catalyst (100 mg catalyst in 100 mL water). After 6 h of illumination, the total incident power over the 9 cm^2 irradiation area was 1.53 W, so that the total input energy in 6 h was:

$$E_{\text{Solar}} = 1.836 \times 10^4\text{ J}$$

During the photocatalytic reaction, $38.6\text{ }\mu\text{mol}$ H_2 was detected by gas chromatography (GC), which indicated that the energy generated by water splitting is:

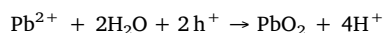
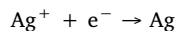
$$E_F = 18.44\text{ J}$$

The solar-to-hydrogen conversion efficiency (STH) of NCN/CDs-1000 ($0.025\text{ g}_{\text{CDs}}/\text{g}_{\text{catalyst}}$) was determined to be:

$$STH = E_F/E_{\text{Solar}} = 18.44\text{ J}/1.836 \times 10^4 = 0.1\%$$

2.8. Determination of reduction sites and oxidation sites

It has been reported that Ag particles would be photodeposited on reduction sites and PbO_2 particles on oxidation sites. The reactions are shown as follows:



In our work, 2 mg catalyst powder was dispersed in 30 mL of ultrapure water, and the suspension was then irradiated by a 300 W Xe-lamp for 3 h under continuous stirring. Subsequently, 0.5 mg $AgNO_3$ [or $Pb(NO_3)_2$] powder was added to the above suspension and continuously stirred for 30 min in darkness. The intermixture was then centrifuged to obtain the solid products and further analyzed by HRTEM to determine the reduction sites (or oxidation sites) where the Ag (or PbO_2) deposited.

2.9. Hydrogen peroxide (H_2O_2) generation test

To detect whether H_2O_2 was formed during the photocatalytic water splitting process. The liquid supernatant was detected by UV-vis spectroscopy using *o*-tolidine as the peroxide indicator. By centrifugalizing the catalyst suspension at 8000 rpm for 2 min, 3 mL of liquid supernatant was collected, and then 1 mL 1% *o*-tolidine dissolved in 0.1 M HCl was added. Finally, UV-vis absorption spectrometer was used to characterize whether the mixture shows a peak at 437 nm, which is the typical peak generated by H_2O_2 .

3. Results and discussion

3.1. Characterization of photocatalysts

The characterization results shown in Figs. S1-S3 suggest that CDs are monodispersed graphite particles ($\sim 5\text{ nm}$ in average) with abundant surface functional groups like $-OH$ and $-COOH$ [30]. The general schematic diagram of preparing NCN/CDs photocatalysts is illustrated in Fig. S4. Firstly, aniline, the mixture of ammonium persulfate (APS), hydrochloric acid (HCl) and CDs are injected into a beaker and mixed uniformly via vigorous stirring within several minutes (Fig. S4a,b). Secondly, a piece of cleaned MF with dense network structure (Fig. S5) is put into the beaker to adsorb the mixing solution (Fig. S4c). After that, the wet MF with mixture is put standing under room conditions for 3 days (Fig. S4d,e) to form the N-doped precursor. Finally, the catalysts with carbon defects are produced by pyrolyzing the precursor in a tube furnace under different temperature ranging from 600 to 1100°C with an interval of 100°C (Fig. S4f). The obtained photocatalysts are denoted from NCN/CDs-600 to NCN/CDs-1100, respectively. A series of control samples without CDs were also prepared for comparison, which are marked as NCN-600 to NCN-1100. Other control samples made from MF (M-1000), PANI (P-1000), MF + CDs (MC-1000) and PANI + CDs (PC-1000) were manufactured by direct pyrolysis under 1000°C with other conditions invariant. The characterization and discussion in the main text are focused on NCN/CDs-1000 since it exhibits the best photocatalytic properties. Supporting materials provide the characterizations of other samples.

The precursor undergoes an evident morphological transformation during the pyrolytic process. At the beginning, the precursor is uniformly wrapped with PANI nanosheets but maintains the netlike structure of pure MF (Fig. S6), confirming that PANI is firmly integrated with the MF substrate. After pyrolysis, the morphological structure of NCN/CDs-1000 (the optimized samples) is entirely different (Fig. S7a), since the netlike structure has been destroyed with only short fibers left. It is notable that short fibers have very rough surfaces (Fig. S7b) compared to the precursor, which is beneficial for photocatalytic overall water splitting.

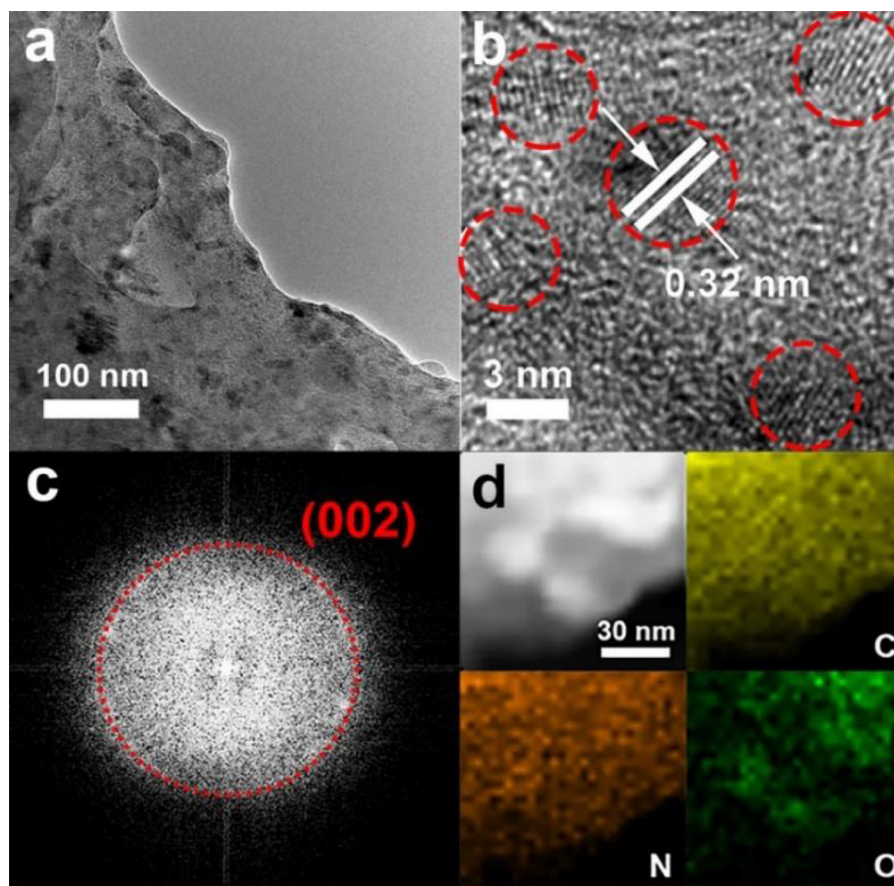


Fig. 1. Electron microscopic characterization of NCN/CDs-1000 photocatalyst. (a–c) TEM, HRTEM and the corresponding FFT images of the photocatalyst. (d) HAADF-STEM image and elemental mappings of the photocatalyst.

TEM image (Fig. 1a) reveals the embedding of nano-particles and the rough surface of NCN/CDs-1000. A magnified TEM image (Fig. 1b) indicates the uniform distribution of CDs nanocrystallites with interplanar spacing of 0.32 nm, which corresponds to the (002) interlayer spacing of graphitic carbon. A 2D fast Fourier transform (FFT) pattern derived from Fig. 1b exhibits a legible round of diffraction points, which are also consistent with the orientation of 0.32 nm crystallites (Fig. 1c). As shown in Fig. S8, NCN-1000 is structurally similar to NCN/CDs-1000 while the SEM images of M-1000, P-1000 (Figs. S9–S10) appear completely different morphology from that of NCN/CDs-1000, which again emphasizes the significance of the precursor. TEM images taken from P-1000, M-1000 and NCN-1000 display the amorphous states of the precise structure (Fig. S11), illustrating no nanocrystals. The elemental mappings (Fig. 1d) taken from the HAADF-STEM indicate there are only C, N and O in the samples. It is noteworthy that the control samples including M-1000, P-1000, MC-1000, PC-1000 and the precursor have no photocatalytic activity under visible light irradiation, whereas NCN-1000 shows very weak photocatalytic activity under the same conditions. In consequence, the rough fiber structure and carbon nanocrystals embedded inside are supposed to play extremely important roles in the photocatalytic performance.

The crystal textures of NCN/CDs-600 to NCN-/CDs-1100 are identified by the XRD patterns (Fig. S12). All the six samples show two broad peaks at around 26° and 43° indexed to the spacing of 0.32 nm and 0.21 nm of graphite, which have illustrated the fine graphitic structure of the synthesized samples. Two characteristic peaks centred at 1332.7 and 1582.2 cm^{-1} were observed for Raman spectra (Fig. S13), which correspond to the D band of defects and G band of sp^2 carbon, respectively [31,32]. FTIR spectroscopy was carried out in order to identify the types of the chemical bonds in the photocatalysts.

The FTIR spectra (Fig. S14) were acquired with several absorption bands situated at 3428 , 1628 , and 1052 cm^{-1} which are assigned to the vibrational modes of OH, C=O and C–O–C, respectively [32,33]. These oxygen-containing moieties are mostly originated from the surface functional groups of CDs. Moreover, the peak at about 1384 cm^{-1} is ascribed to the C–N stretching vibrations and demonstrates the nitrogen doping of the photocatalyst [34,35]. The BET surface areas and average pore sizes are listed in Table S1, manifesting that the BET surface area is boosted upon the temperature rising with NCN/CDs-1000 owning the largest BET surface area. The exceptional decrease for NCN/CDs-1100 results from the structural collapse or reconstruction under excessive temperature.

Further analyses of the chemical states and elemental compositions of the samples are shown in the XPS spectra. The full spectra of NCN/CDs photocatalysts are provided in Fig. S15, in which only the signals of C, N and O can be observed. The high resolution C 1s spectra are normally deconvoluted into four peaks located at around 284.6, 285.8, 286.7 and 288.8 eV, corresponding to C–C, C–N, C–O and C=O bonds, respectively [36,37]. The fitted peaks of N 1s spectra at about 398.2 and 400.8 eV are assigned to pyridinic and graphitic nitrogen, respectively [38]. It is notable that the nitrogen content gradually decreases from 16.2% to 1.29% with the removal temperature increasing from 600 to 1100°C , while the oxygen content stays similar for all the samples (Table S2). The elemental compositions derived from C 1s and N 1s spectra are listed below Fig. S15.

For the sake of carefully illustrating the nitrogen changes after the removal process, the merged C 1s and N 1s spectra over NCN/CDs-600 to NCN/CDs-1100 are shown in Fig. 2. It is apparent that the C–C peak remains almost unchanged, while the C–N peak continuously decreases with the increased temperature (Fig. 2a). The N content is also

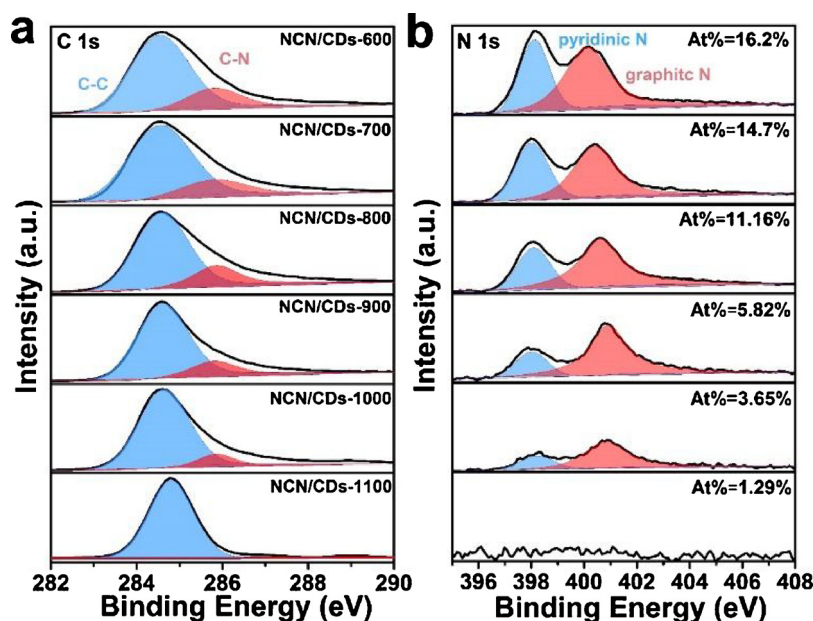


Fig. 2. Surface chemical states and elemental compositions of NCN/CDs-1000. Merged XPS (a) C 1s spectra and (b) N 1s spectra of NCN/CDs-600 to NCN/CDs-1100.

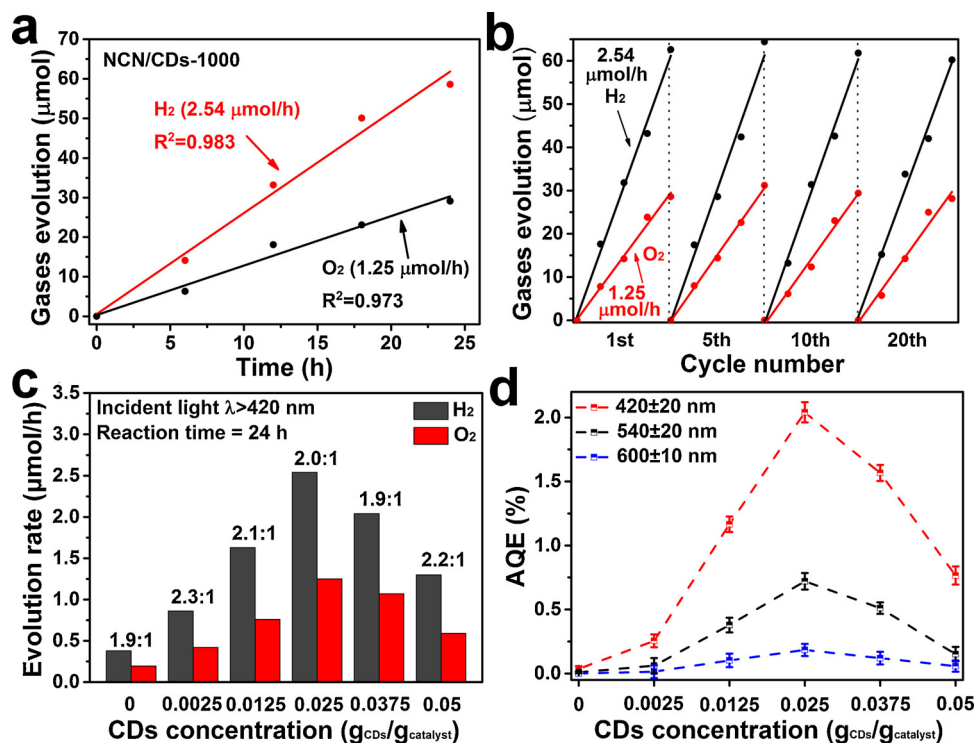


Fig. 3. Photocatalytic properties of NCN/CDs-1000. (a,b) Typical time course of H_2 (O_2) production and stability of NCN/CDs-1000. (c,d) Gases production and apparent quantum efficiency (AQE) of NCN/CDs-1000 with different CDs concentration for 0, 0.0025, 0.0125, 0.025, 0.0375 and 0.05 $\text{g}_{\text{CDs}}/\text{g}_{\text{catalyst}}$ (catalyst loading content in ultrapure water is 1 mg mL^{-1}).

decreasing sharply with the increased temperature (Fig. 2b). NCN/CDs-1000 has the lowest percentage of N element, while NCN/CDs-600 has the highest. Note the N content of NCN/CDs-1100 is too low (only 1.29%) to be quantified precisely in the N 1s spectrum. The XPS results suggest that the removal of nitrogen atoms could be the fundamental reason for the formation of defects, and the amount of defects can grow by removing nitrogen under higher temperature. This result is consistent with recent reports for producing carbon defects [39–41]. Interestingly, the photocatalytic activity is proportional to the number of defects (inversely proportional to nitrogen content) except for NCN/CDs-1100 (Fig. 3). The lower activity of NCN/CDs-1100 can be attributed to the excessively high temperature, which will lead to the reconstruction of the carbon lattice rings and adversely reduce the defects

[42–44]. By creating more defects, the optimal activity is 10 times over the non-optimized catalyst (few defects). Table S3 has shown the elemental compositions stemming from the combustion method which exhibits the same trend with XPS data (note that the trace amount of S is originated from the residual APS which is very hard to be completely removed).

3.2. Photocatalytic property of photocatalysts

To investigate the photocatalytic properties and stability of the photocatalysts, procedural experiments were implemented. UV–vis DRS spectra of NCN/CDs photocatalysts illustrate the photocatalysts can make use of wide range of visible light in virtue of the strong absorption

in the visible light range (Fig. S16). During 24 h photocatalytic reaction (Fig. 3a) for NCN/CDs-1000 in ultrapure water, the H_2 and O_2 evolution proceeds continuously in a molar ratio of 2:1 for H_2/O_2 (2.54 and $1.25 \mu\text{mol h}^{-1}$, respectively), which is identical to the theoretical value of 2 for overall water splitting. The stability of NCN/CDs-1000 was evaluated by cyclic experiments and during each time was 24 h irradiation under visible light ($\lambda > 420 \text{ nm}$). As is manifested in Fig. 3b, it is conspicuous that the catalyst shows stable production of H_2/O_2 and still keeps 93% of the initial activity after 20 times usage. The optimal loading content for catalyst adding to water was estimated by the AQE values. The initial increase (Fig. S17) of the catalyst loading content increases the AQE until reaching a maximum, but the AQE remains nearly unchanged when further increasing the adding quantity.

An additional experiment was performed likewise to probe the relevance between the concentrations of added CDs and the photocatalytic properties of NCN/CDs-1000. The control constituents were prepared using the same quantity of raw materials except for the CDs content. The results in Fig. 3c-d suggest that $0.025 \text{ g}_{\text{CDs}}/\text{g}_{\text{catalyst}}$ is the optimal concentration of CDs with respect to the highest gases production (Fig. 3c) and AQE (Fig. 3d). Specifically, if no CDs is involved, NCN-1000 ($0 \text{ g}_{\text{CDs}}/\text{g}_{\text{catalyst}}$) shows very low photocatalytic properties which is probably due to the fast recombination of the electron-hole pairs (Fig. S18). The photocatalytic activity is proportional to CDs content when it rises from 0 to $0.025 \text{ g}_{\text{CDs}}/\text{g}_{\text{catalyst}}$, yet when CDs concentration is higher than $0.025 \text{ g}_{\text{CDs}}/\text{g}_{\text{catalyst}}$, the activity turns to decline which might be caused by the partial agglomeration of CDs or the coverage of the active sites inside the matrix. Fig. S19 has offered a group of HRTEM images showing the reduction sites (Ag particles deposited, spacing of 0.23 nm) and oxidation sites (PbO_2 particles deposited, spacing of 0.35 nm) over NCN/CDs-1000. It demonstrates that the photocatalysts have both oxidation sites for O_2 production (away from CDs) and reduction sites for H_2 production (on CDs).

3.3. Electrochemical band structure of the photocatalysts

Based on the results above, the modulation of the temperature could remove the nitrogen to create defects for photocatalytic reaction. With the purpose of evaluating the HOMO and LUMO positions, cyclic voltammetry (CV) experiments were conducted to determine the highest occupied molecular orbital (HOMO) and lowest unoccupied molecular orbital (LUMO) positions (equivalent to the valence band (VB) and the conduction band (CB), respectively). Fig. S20 provides the CV curves of NCN/CDs-600 to NCN/CDs-1100, where the ferrocene redox system was introduced as an external standard. Each curve possesses two pairs of redox peaks with one pair from the commercial ferrocene and the other from the catalyst itself. According to Eqs. (1–3), the onset of oxidation (E_{ox}) and reduction (E_{red}) potentials were measured respectively, and the reference energy level for ferrocene (4.8 eV below the vacuum level) was also obtained (Table 1). As shown in Fig. 4, the measured LUMO and HOMO of NCN/CDs-900 to NCN/CDs-1100 all straddled the reduction and oxidation potentials of water at $+0$ and $+1.23 \text{ V}$ versus the reversible hydrogen electrode (RHE), respectively. On the contrary, NCN/CDs-600 to NCN/CDs-800 have a HOMO below

the oxidation potentials of water at $+1.78 \text{ V}$ (vs. RHE). Consequently, it is feasible to theoretically split water into H_2 and O_2 via a direct 4-electron pathway using NCN/CDs-900 to NCN/CDs-1100 while via a 2-electron pathway to get H_2 and H_2O_2 using NCN/CDs-600 to NCN/CDs-800. In the meantime, NCN-600 to NCN-1100 (Table S4) also exhibit the similar electrochemical band positions which means the electrochemical band positions are mainly influenced by the nitrogen content.

3.4. Comparison of photocatalytic properties

Fig. 4b shows the photocatalytic gases generation over NCN/CDs-600 to NCN/CDs-1100 with the optimum conditions. According to Fig. 4b, all the six photocatalysts can split water into both H_2 and O_2 in the stoichiometric ratio of approximately 2:1. Generally speaking, the increase of defects (removal of more nitrogen) enhances the activity towards photocatalytic overall water splitting with the highest gained for NCN/CDs-1000, which is 10 times of that of NCN/CDs-600. NCN/CDs-1100 is less active than NCN/CDs-900 because the rearrangement of carbon atoms under excessive temperature might conversely reduce the inchoate defects. The optimal overall gases production of NCN-600 to NCN-1100 and typical time course gases production of NCN/CDs-600 and NCN-600 are provided in Figs. S21–22. It is apparent that all the photocatalysts can split water into H_2 and O_2 in the ratio close to 2:1 in spite of the low production (NCN-1000 is the highest with H_2 $0.38 \mu\text{mol h}^{-1}$ and O_2 $0.2 \mu\text{mol h}^{-1}$), yet it still confirms that more defects could enhance the photocatalytic activity. To have a better estimation on the photocatalytic activity of NCN/CDs-600 to NCN/CDs-1100, AQE values were tested at different wavelengths (Fig. 4c). The increase of the wavelength causes decrease of AQE. Particularly, NCN/CDs-1000 shows the highest AQE through all the specified wavelengths compared to the other catalysts, which exhibits the values of 2.04% at $420 \pm 20 \text{ nm}$, 0.72% at $540 \pm 20 \text{ nm}$, and 0.18% at $600 \pm 10 \text{ nm}$. When irradiation wavelength reaches 650 nm , no AQE is achieved.

The EIS experiments were conducted to appraise the photo-induced charge transfer ability of the photocatalysts which is very important for water decomposition. As reported by many researchers, a smaller semicircle in an EIS Nyquist plot means an easier trend for the electrons to be transferred to the protons in the electrolyte from the conduction band of materials [45]. It can be easily observed (Fig. S23a), except for NCN/CDs-1100, NCN/CDs-1000 has the smallest semicircle over the others, on the other hand, NCN/CDs-600 has the largest semicircle and others fall in between. Note even NCN/CDs-1100 has a smaller impedance arc than that of NCN/CDs-1000 due to the carbon rearrangement as well as reduction of defects, which, however, makes no contribution to the photocatalytic activity. The EIS data offered in Fig. S23b for NCN samples also demonstrate the same trend but all have larger semicircles. The EIS results are consistent with the photocatalytic activities obtained. The photoluminescence (PL) spectra of the photocatalysts displayed in Fig. S24 suggest that the charge recombination is more substantially suppressed if the photocatalytic activity is higher, which is in good agreement with the EIS data. The results have confirmed the introduction of CDs dramatically enhances the photocatalytic activity owing to the improved charge transfer, suppressed charge recombination as well as increased reduction sites.

3.5. Study on the electron transfer number

As characterized previously, the HOMO moves positively when the removal temperature is increasing. Therefore, the 2-electron/2-electron pathway has been forced to 4-electron transfer pathway. RRDE measurements were carried through to verify the actual electron transfer number (Fig. S25). According to the RRDE plots of NCN/CDs-900 to NCN/CDs-1100, the disk current appears a sharp ascent while the ring current manifests nearly no saltation after light irradiation, demonstrating that no H_2O_2 is detected under light irradiation. The electron transfer numbers are calculated close to 4, which agrees with the

Table 1

Nitrogen content (NC) from XPS, E_{HOMO} (eV), E_{LUMO} (eV), Electrochemical band Gap (EBG) and electron transfer number (n) over NCN/CDs-600 to NCN/CDs-1100.

	NC (%)	E_{HOMO} (eV)	E_{LUMO} (eV)	EBG (eV)	n
NCN/CDs-600	16.2	−6.3	−4.23	2.07	2.1
NCN/CDs-700	14.7	−6.28	−4.27	2.01	2.8
NCN/CDs-800	11.16	−6.25	−4.21	2.04	3.2
NCN/CDs-900	5.82	−6.1	−4.22	1.88	3.7
NCN/CDs-1000	3.65	−6.08	−4.12	1.96	3.9
NCN/CDs-1100	1.29	−6.02	−4.01	2.01	3.8

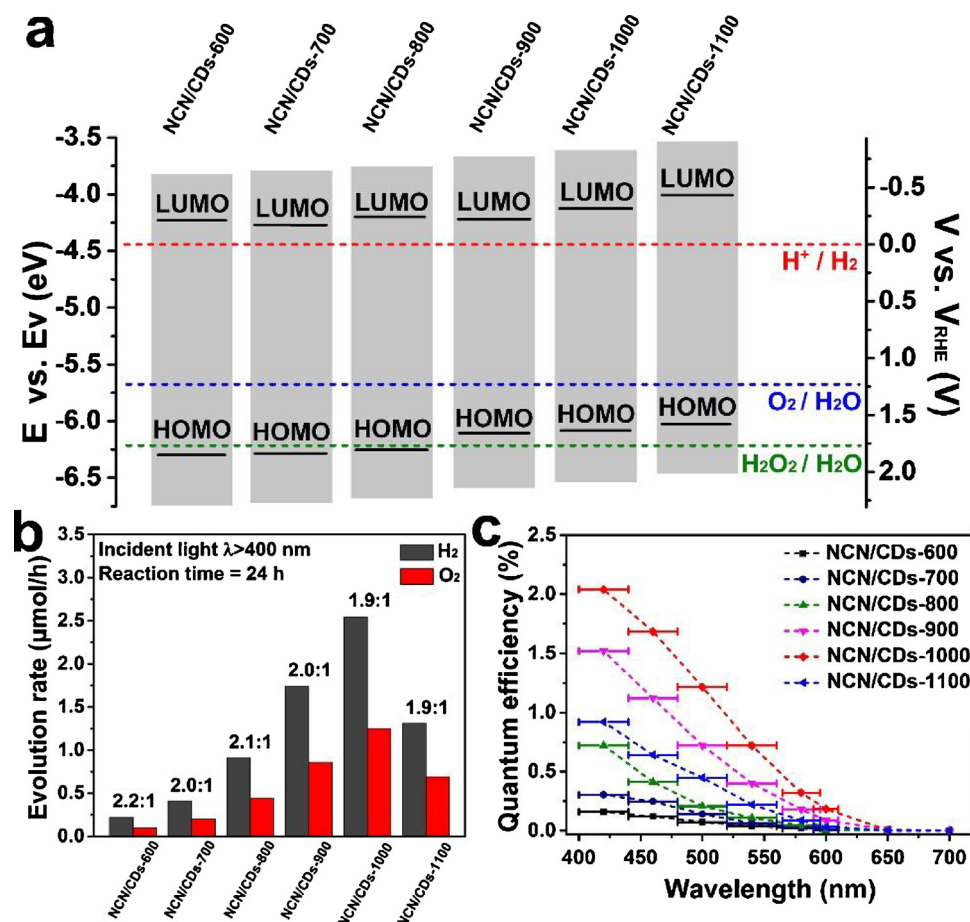


Fig. 4. HOMO-LUMO structure and photocatalytic properties of the catalysts. (a) HOMO-LUMO structure diagram; (b) gases evolution rates and (c) AQE under different wavelengths of NCN/CDs-600 to NCN/CDs-1100.

theoretical results of band edges (Table 1). In contrast, the electron transfer numbers of NCN/CDs-600 to NCN/CDs-800 are calculated to be 2.1, 2.8 and 3.2, respectively (Table 1), showing a shift from 2-electron/2-electron pathway to the 4-electron pathway. Moreover, the electron transfer numbers obtained for NCN samples (Table S4) have similar results, correlating to the inference that the electron transfer number of the photocatalysts is mainly influenced by the nitrogen content. The photocatalysts with 4-electron pathway indeed show higher activity than those with 2-electron pathway, which supports the statement that four-electron process is thermodynamically superior to the two-electron process.

The H_2O_2 accumulation is evaluated through the UV-vis spectra of reaction solutions containing 1% *o*-tolidine (Fig. S26). In particular, the standard solution containing H_2O_2 has a prominent peak at 437 nm, in opposite, the reaction solutions from all the photocatalysts exhibit no peaks at the same wavelength, revealing that all the H_2O_2 produced was decomposed (NCN/CDs-600 to NCN/CDs-800) or no H_2O_2 was produced (NCN/CDs-900 to NCN/CDs-1100). Similarly, UV-vis spectra of accumulated H_2O_2 over NCN-600 to NCN-1100 (Fig. S27) exert the same consequences. The capacity of CDs, NCN and NCN/CDs samples decomposing H_2O_2 is presented in Fig. S28 and Table S5, all of which show fine ability to decompose H_2O_2 into O_2 . This explains why NCN-600 to NCN-800 also produce H_2 and O_2 in the stoichiometric rate of 2:1 and UV-vis spectra of H_2O_2 accumulation show no peak at 437 nm. By reason of the close proximity between the components during the preparation, the introduction of CDs into the matrix also improves the decomposition ability towards H_2O_2 into O_2 .

On the basis of the comprehensive results above, the modulation mechanism of the NCN/CDs is summarized. When the annealing

temperature increases from 600 to 800 °C, the nitrogen content decreases from 16.2% to 11.2% and the HOMO moves positively but still lies below the oxidation potential of H_2O_2 . Meanwhile, the electron transfer number shows a transformation from the stepwise 2-electron/2-electron process to a concomitant process. When the temperature increases from 900 to 1100 °C, the nitrogen content further decreases from 5.8% to 1.3% with the HOMO moving further which only meets the 4-electron pathway. The calculated electron transfer number also verifies the 4-electron pathway. The photocatalytic activity generally displays a negative correlation with the nitrogen content as the removal of nitrogen generates defects as active sites for the catalytic reaction. Another possibility for the boosted activity is that the removal of nitrogen reduces the activation energy required and improves surface reaction kinetics, which simultaneously lowers the barrier to photocatalysis.

The removal of nitrogen to create carbon defects can be revealed by the X-ray absorption spectroscopy (XAS) results in Fig. 5a. The XAS spectrum of NCN/CDs-1000 before photocatalytic reaction shows two main peaks at 285.5 eV and 292.0 eV responsible for the π^* and σ^* excitation of C–C bonds in a carbon ring structure, respectively[46,47]. A weak feature at 288.7 eV can be also observed (The NCN-1000 sample without CDs also shows similar spectra, data not shown)[46,47]. However, after photocatalytic reaction for the same sample, a prominent feature at 288.7 eV can be observed revealing the formation of large amounts of oxidized carbon such as C–OH or COOH. The easily oxidized nature of NCN/CDs-1000 strongly suggests the presence of abundant defects. The defects may also be the active sites to bond oxygen species and then produce O_2 in the photocatalytic reaction. The bonding of oxygen species with the defected carbon is also confirmed

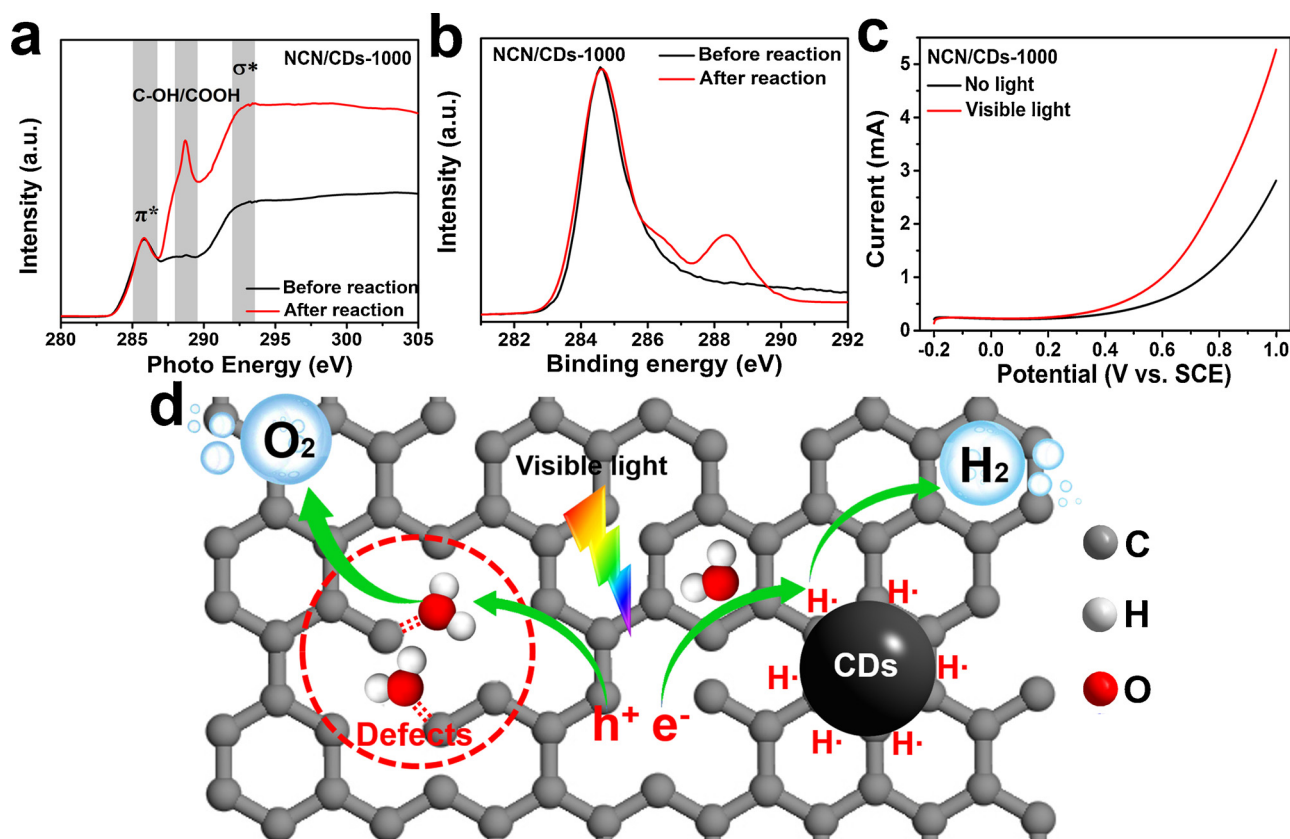


Fig. 5. Exploration on photocatalytic reaction mechanism. (a) XAS spectra of NCN/CDs-1000 before and after water splitting reaction. (b) XPS spectra of NCN/CDs-1000 before and after water splitting reactions. (c) Linear sweep voltammetry (LSV) curves of NCN/CDs-1000 with and without light irradiation in 1 M KOH solution. (d) Proposed schematic diagram of the photocatalytic reaction process.

by the XPS spectra (Fig. 5b), namely two distinct peaks at 286.6 and 288.6 eV in the XPS spectrum of the sample after reaction possesses, while the peaks are weak in the initial spectrum. Additionally, the electrochemical test is conducted with adsorbed light irradiation when scanning the oxygen evolution reaction (OER) curves for NCN/CDs-1000. The OER current undergoes a significant enhancement in the high potential range (0.8–1.0 V vs. SCE) as the bonded oxygen species in defected areas assist the electrochemical OER process (Fig. 5c).

A tentative mechanism for the photocatalysts is proposed (Fig. 5d). At the beginning, water adsorbs on the surface of the photocatalysts (especially around the defects). When the photocatalysts are irradiated under visible light, electron-hole pairs can be produced in the defect-rich catalysts due to the favorable molecular orbitals. Then, holes (h^+) can migrate to the defect sites and react with the adsorbed water molecules to produce O_2 , either directly into O_2 via 4-electron pathway or into H_2O_2 by 2-electron pathway. The generated electrons (e^-) can easily transfer to the surface of CDs as they are fine electron acceptors, and then produce H_2 on CDs. Hence, the charge carriers are well separated with the presence of both defects and CDs for overall water splitting. Spontaneously, if it proceeds the stepwise 2-electron pathway, the catalyst also decomposes H_2O_2 into H_2O and O_2 so as to maintain the H_2 and O_2 production to be 2:1.

4. Conclusions

In general, an active carbon-based metal-free photocatalyst was prepared with abundant defects by facily removing the nitrogen atoms from a N-doped precursor. The photocatalytic activity can increase for about 10 times by creating more defects. The photocatalysts can split water either via the 4-electron pathway (nitrogen content more than 10%) or stepwise 2-electron/2-electron dominant pathway

(nitrogen content less than 10%) with H_2 and O_2 production in the stoichiometric ratio of 2:1. The systematic study has validated that carbon defects are the oxidation sites for O_2 generation, while CDs act as reduction sites for H_2 evolution. Besides, the photocatalysts also show an AQE of $2.04\% \pm 20$ nm and STH efficiency of 0.1%. This work provides a facile and practical method to produce metal-free carbon catalysts with activated defects, which offer a new approach for developing carbon based materials in both photochemical and photoelectrochemical applications.

Conflict of interest

The authors declare no competing financial interest.

Acknowledgment

This work is supported by the Collaborative Innovation Center of Suzhou Nano Science and Technology, the National Natural Science Foundation of China (51725204, 51572179, 21471106, 21771132, 21501126), the Natural Science Foundation of Jiangsu Province (BK20161216) and a project funded by the Priority Academic Program Development of Jiangsu Higher Education Institutions (PAPD).

Appendix A. Supplementary data

Supplementary material related to this article can be found, in the online version, at doi:<https://doi.org/10.1016/j.apcatb.2018.05.071>.

This material is available free of charge via the Internet at <https://www.journals.elsevier.com/nano-energy/>.

References

- [1] A.J. Bard, M.A. Fox, Artificial photosynthesis: solar splitting of water to hydrogen and oxygen, *Acc. Chem. Res.* 28 (1995) 141–145, <http://dx.doi.org/10.1021/ar00051a007>.
- [2] A. Kudo, Y. Miseki, Heterogeneous photocatalyst materials for water splitting, *Chem. Soc. Rev.* 38 (2009) 253–278, <http://dx.doi.org/10.1039/B800489G>.
- [3] K. Maeda, K. Domen, Photocatalytic water splitting: recent progress and future challenges, *J. Phys. Chem. Lett.* 1 (2010) 2655–2661, <http://dx.doi.org/10.1021/jz1007966>.
- [4] S. Iida, T. Ishihara, Recent progress in Two-dimensional oxide photocatalysts for Water splitting, *J. Phys. Chem. Lett.* 5 (2014) 2533–2542, <http://dx.doi.org/10.1021/jz5010957>.
- [5] S. Chen, T. Takata, K. Domen, Particulate photocatalysts for overall water splitting, *Nat. Rev. Mater.* 2 (2017) 17050, <http://dx.doi.org/10.1038/natrevmats.2017.50>.
- [6] J. Xing, W.Q. Fang, H.J. Zhao, H.G. Yang, Inorganic photocatalysts for overall water splitting, *Chem.-Asian J.* 7 (2012) 642–657, <http://dx.doi.org/10.1002/asia.201100772>.
- [7] K. Takanabe, K. Domen, Preparation of inorganic photocatalytic materials for overall Water splitting, *ChemCatChem* 4 (2012) 1485–1497, <http://dx.doi.org/10.1002/cctc.201200324>.
- [8] Tsuyoshi Takata, Akira Tanaka, Michikazu Hara, Junko Kondo, Kazunari Domen, Recent progress of photocatalysts for overall water splitting, *Catal. Today* 44 (1998) 17–26.
- [9] L. Liao, Q. Zhang, Z. Su, Z. Zhao, Y. Wang, Y. Li, X. Lu, D. Wei, G. Feng, Q. Yu, X. Cai, J. Zhao, Z. Ren, H. Fang, F. Robles-Hernandez, S. Baldelli, J. Bao, Efficient solar water-splitting using a nanocrystalline CoO photocatalyst, *Nat. Nanotechnol.* 9 (2013) 69–73, <http://dx.doi.org/10.1038/nnano.2013.272>.
- [10] X. Chen, S. Shen, L. Guo, S.S. Mao, Semiconductor-based photocatalytic hydrogen generation, *Chem. Rev.* 110 (2010) 6503–6570, <http://dx.doi.org/10.1021/cr1001645>.
- [11] S.J.A. Moniz, S.A. Shevlin, D.J. Martin, Z.-X. Guo, J. Tang, Visible-light driven heterojunction photocatalysts for water splitting – a critical review, *Energy Environ. Sci.* 8 (2015) 731–759, <http://dx.doi.org/10.1039/C4EE03271C>.
- [12] K. Maeda, Z-Scheme water splitting using two different semiconductor photocatalysts, *ACS Catal.* 3 (2013) 1486–1503, <http://dx.doi.org/10.1021/cs4002089>.
- [13] T. Hisatomi, J. Kubota, K. Domen, Recent advances in semiconductors for photocatalytic and photoelectrochemical water splitting, *Chem. Soc. Rev.* 43 (2014) 7520–7535, <http://dx.doi.org/10.1039/C3CS60378D>.
- [14] G. Zhang, Z.-A. Lan, X. Wang, Surface engineering of graphitic carbon nitride polymers with cocatalysts for photocatalytic overall water splitting, *Chem. Sci.* 8 (2017) 5261–5274, <http://dx.doi.org/10.1039/C7SC01747B>.
- [15] C. Li, Y. Xu, W. Tu, G. Chen, R. Xu, Metal-free photocatalysts for various applications in energy conversion and environmental purification, *Green Chem.* 19 (2017) 882–899, <http://dx.doi.org/10.1039/C6GC02856J>.
- [16] T.-F. Yeh, F.-F. Chan, C.-T. Hsieh, H. Teng, graphite oxide with different oxygenated levels for hydrogen and oxygen production from water under illumination: the band positions of graphite oxide, *J. Phys. Chem. C* 115 (2011) 22587–22597, <http://dx.doi.org/10.1021/jp204856c>.
- [17] T.-F. Yeh, S.-J. Chen, C.-S. Yeh, H. Teng, Tuning the electronic structure of graphite oxide through ammonia treatment for photocatalytic generation of H_2 and O_2 from Water splitting, *J. Phys. Chem. C* 117 (2013) 6516–6524, <http://dx.doi.org/10.1021/jp312613r>.
- [18] J. Liu, Y. Liu, N. Liu, Y. Han, X. Zhang, H. Huang, Y. Lifshitz, S.-T. Lee, J. Zhong, Z. Kang, Metal-free efficient photocatalyst for stable visible water splitting via a two-electron pathway, *Science* 347 (2015) 967–970, <http://dx.doi.org/10.1126/science.aaa5760>.
- [19] K. Zhang, L. Wang, X. Sheng, M. Ma, M.S. Jung, W. Kim, H. Lee, J.H. Park, Tunable bandgap energy and promotion of H_2O_2 oxidation for overall Water splitting from carbon nitride nanowire bundles, *Adv. Energy Mater.* 6 (2016) 1502352, <http://dx.doi.org/10.1002/aenm.201502352>.
- [20] L. Wang, Y. Wan, Y. Ding, S. Wu, Y. Zhang, X. Zhang, G. Zhang, Y. Xiong, X. Wu, J. Yang, H. Xu, Conjugated microporous polymer nanosheets for overall Water splitting using visible light, *Adv. Mater.* 29 (2017) 1702428, <http://dx.doi.org/10.1002/adma.201702428>.
- [21] D. Yan, Y. Li, J. Huo, R. Chen, L. Dai, S. Wang, Defect chemistry of nonprecious-metal electrocatalysts for oxygen reactions, *Adv. Mater.* (2017) 1606459, <http://dx.doi.org/10.1002/adma.201606459>.
- [22] L. Tao, Q. Wang, S. Dou, Z. Ma, J. Huo, S. Wang, L. Dai, Edge-rich and dopant-free graphene as a highly efficient metal-free electrocatalyst for the oxygen reduction reaction, *Chem. Commun.* 52 (2016) 2764–2767, <http://dx.doi.org/10.1039/C5CC09173J>.
- [23] X. Pan, M.-Q. Yang, X. Fu, N. Zhang, Y.-J. Xu, Defective TiO_2 with oxygen vacancies: synthesis, properties and photocatalytic applications, *Nanoscale* 5 (2013) 3601, <http://dx.doi.org/10.1039/c3nr00476g>.
- [24] D. Chen, Z. Wang, T. Ren, H. Ding, W. Yao, R. Zong, Y. Zhu, Influence of defects on the photocatalytic activity of ZnO , *J. Phys. Chem. C* 118 (2014) 15300–15307, <http://dx.doi.org/10.1021/jp5033349>.
- [25] H. Yu, R. Shi, Y. Zhao, T. Bian, Y. Zhao, C. Zhou, G.I.N. Waterhouse, L.-Z. Wu, C.-H. Tung, T. Zhang, Alkali-assisted synthesis of nitrogen deficient graphitic carbon nitride with tunable band structures for efficient visible-light-driven hydrogen evolution, *Adv. Mater.* 29 (2017) 1605148, <http://dx.doi.org/10.1002/adma.201605148>.
- [26] X. Li, G. Hartley, A.J. Ward, P.A. Young, A.F. Masters, T. Maschmeyer, hydrogenated defects in graphitic carbon nitride nanosheets for improved photocatalytic hydrogen evolution, *J. Phys. Chem. C* 119 (2015) 14938–14946, <http://dx.doi.org/10.1021/acs.jpcc.5b03538>.
- [27] V.W. Lau, I. Moudrakovski, T. Botari, S. Weinberger, M.B. Mesch, V. Duppel, J. Senker, V. Blum, B.V. Lotsch, Rational design of carbon nitride photocatalysts by identification of cyanamide defects as catalytically relevant sites, *Nat. Commun.* 7 (2016) 12165, <http://dx.doi.org/10.1038/ncomms12165>.
- [28] C. Zhu, Y. Fu, C. Liu, Y. Liu, L. Hu, J. Liu, I. Bello, H. Li, N. Liu, S. Guo, H. Huang, Y. Lifshitz, S.-T. Lee, Z. Kang, Carbon dots as fillers inducing healing/self-healing and anticorrosion properties in polymers, *Adv. Mater.* 29 (2017) 1701399, <http://dx.doi.org/10.1002/adma.201701399>.
- [29] C. Zhu, C. Liu, Y. Zhou, Y. Fu, S. Guo, H. Li, S. Zhao, H. Huang, Y. Liu, Z. Kang, Carbon dots enhance the stability of CdS for visible-light-driven overall water splitting, *Appl. Catal. B: Environ.* 216 (2017) 114–121, <http://dx.doi.org/10.1016/j.apcatb.2017.05.049>.
- [30] H. Ming, Z. Ma, Y. Liu, K. Pan, H. Yu, F. Wang, Z. Kang, Large scale electrochemical synthesis of high quality carbon nanodots and their photocatalytic property, *Dalton Trans.* 41 (2012) 9526, <http://dx.doi.org/10.1039/c2dt30985h>.
- [31] H. Li, X. He, Z. Kang, H. Huang, Y. Liu, J. Liu, S. Lian, C.H.A. Tsang, X. Yang, S.-T. Lee, Water-soluble fluorescent carbon quantum dots and photocatalyst design, *Angew. Chem. Int. Ed.* 49 (2010) 4430–4434, <http://dx.doi.org/10.1002/anie.200906154>.
- [32] H. Li, Z. Kang, Y. Liu, S.-T. Lee, Carbon nanodots: synthesis, properties and applications, *J. Mater. Chem.* 22 (2012) 24230, <http://dx.doi.org/10.1039/c2jm34690g>.
- [33] X.T. Zheng, A. Ananthanarayanan, K.Q. Luo, P. Chen, Glowing graphene quantum dots and carbon dots: properties, syntheses, and biological applications, *Small* 11 (2015) 1620–1636.
- [34] W. Wei, C. Xu, L. Wu, J. Wang, J. Ren, X. Qu, Non-enzymatic-browning-reaction: a versatile route for production of nitrogen-doped carbon dots with tunable multi-color luminescent display, *Sci. Rep.* 4 (2015), <http://dx.doi.org/10.1038/srep03564>.
- [35] H. Zhang, Y. Chen, M. Liang, L. Xu, S. Qi, H. Chen, X. Chen, Solid-phase synthesis of highly fluorescent nitrogen-doped carbon dots for sensitive and selective probing ferric ions in living cells, *Anal. Chem.* 86 (2014) 9846–9852, <http://dx.doi.org/10.1021/ac502446m>.
- [36] S. Qu, X. Liu, X. Guo, M. Chu, L. Zhang, D. Shen, Amplified spontaneous Green emission and lasing emission from carbon nanoparticles, *Adv. Funct. Mater.* 24 (2014) 2689–2695, <http://dx.doi.org/10.1002/adfm.201303352>.
- [37] M.-S. Balogun, W. Qiu, H. Yang, W. Fan, Y. Huang, P. Fang, G. Li, H. Ji, Y. Tong, A monolithic metal-free electrocatalyst for oxygen evolution reaction and overall water splitting, *Energy Environ. Sci.* 9 (2016) 3411–3416, <http://dx.doi.org/10.1039/C6EE01930G>.
- [38] X. Wu, C. Zhu, L. Wang, S. Guo, Y. Zhang, H. Li, H. Huang, Y. Liu, J. Tang, Z. Kang, Control strategy on two-/four-electron pathway of water splitting by multiphase carbon based catalysts, *ACS Catal.* 7 (2017) 1637–1645, <http://dx.doi.org/10.1021/acscatal.6b03244>.
- [39] H. Zhao, C. Sun, Z. Jin, D.-W. Wang, X. Yan, Z. Chen, G. Zhu, X. Yao, Carbon for the oxygen reduction reaction: a defect mechanism, *J. Mater. Chem. A* 3 (2015) 11736–11739, <http://dx.doi.org/10.1039/C5TA02229K>.
- [40] X. Yan, Y. Jia, T. Odedairo, X. Zhao, Z. Jin, Z. Zhu, X. Yao, Activated carbon becomes active for oxygen reduction and hydrogen evolution reactions, *Chem. Commun.* 52 (2016) 8156–8159, <http://dx.doi.org/10.1039/C6CC03687B>.
- [41] Y. Jia, L. Zhang, A. Du, G. Gao, J. Chen, X. Yan, C.L. Brown, X. Yao, Defect graphene as a trifunctional catalyst for electrochemical reactions, *Adv. Mater.* 28 (2016) 9532–9538, <http://dx.doi.org/10.1002/adma.201602912>.
- [42] J. Kotakoski, A.V. Krashenninnikov, U. Kaiser, J.C. Meyer, From Point defects in graphene to two-dimensional amorphous carbon, *Phys. Rev. Lett.* 106 (2011), <http://dx.doi.org/10.1103/PhysRevLett.106.105505>.
- [43] C. Zhang, L. Fu, N. Liu, M. Liu, Y. Wang, Z. Liu, Synthesis of nitrogen-doped graphene using embedded carbon and nitrogen sources, *Adv. Mater.* 23 (2011) 1020–1024, <http://dx.doi.org/10.1002/adma.201004110>.
- [44] F. Banhart, J. Kotakoski, A.V. Krashenninnikov, Structural defects in graphene, *ACS Nano* 5 (2011) 26–41, <http://dx.doi.org/10.1021/nn102598m>.
- [45] J. Lim, D. Monllor-Satoca, J.S. Jang, S. Lee, W. Choi, Visible light photocatalysis of fullerol-complexed TiO_2 enhanced by Nb doping, *Appl. Catal. B Environ.* 152–153 (2014) 233–240, <http://dx.doi.org/10.1016/j.apcatb.2014.01.026>.
- [46] A. Kuznetsova, I. Popova, J.T. Yates, M.J. Bronikowski, C.B. Huffman, J. Liu, R.E. Smalley, H.H. Hwu, J.G. Chen, Oxygen-containing functional groups on single-wall carbon nanotubes: NEXAFS and vibrational spectroscopic studies, *J. Am. Chem. Soc.* 123 (2001) 10699–10704, <http://dx.doi.org/10.1021/ja011021b>.
- [47] J. Zhong, J.-J. Deng, B.-H. Mao, T. Xie, X.-H. Sun, Z.-G. Mou, C.-H. Hong, P. Yang, S.-D. Wang, Probing solid state N-doping in graphene by X-ray absorption near-edge structure spectroscopy, *Carbon* 50 (2012) 335–338, <http://dx.doi.org/10.1016/j.carbon.2011.08.046>.